

Search and Rescue under the Forest Canopy using Multiple UAVs

Journal Title
XX(X):1–17
©The Author(s) 2019
Reprints and permission:
sagepub.co.uk/journalsPermissions.nav
DOI: 10.1177/ToBeAssigned
www.sagepub.com/

SAGE

Yulun Tian¹, Katherine Liu¹, Kyel Ok¹, Loc Tran², Danette Allen², Nicholas Roy¹ and Jonathan P. How¹

Abstract

We present a multi-robot system for GPS-denied search and rescue under the forest canopy. Forests are particularly challenging environments for collaborative exploration and mapping, in large part due to the existence of severe perceptual aliasing which hinders reliable loop closure detection for mutual localization and map fusion. Our proposed system features unmanned aerial vehicles (UAVs) that perform onboard sensing, estimation, and planning. When communication is available, each UAV transmits compressed tree-based submaps to a central ground station for collaborative simultaneous localization and mapping (CSLAM). To overcome high measurement noise and perceptual aliasing, we use the local configuration of a group of trees as a distinctive feature for robust loop closure detection. Furthermore, we propose a novel procedure based on cycle consistent multiway matching to recover from incorrect pairwise data associations. The returned global data association is guaranteed to be cycle consistent, and is shown to improve both precision and recall compared to the input pairwise associations. The proposed multi-UAV system is validated both in simulation and during real-world collaborative exploration missions at NASA Langley Research Center.

1. Introduction

Lost hikers are often within a mile or two of the last point of detection for extended periods of time, but are undetected for hours because manned aircraft cannot see them through the overhead forest canopy. Instead, a team of small autonomous unmanned aerial vehicles (UAVs) can be deployed *under* the tree canopy to gain better visibility during search and rescue missions in forest areas; these vehicles can be rapidly deployed, can collaboratively explore expanses of terrain efficiently, and are agile enough to operate in reasonably thick forests, such as shown in Figure 1.

Deploying a multi-UAV system for forest search and rescue presents a multitude of technical challenges. Firstly, signals from the Global Positioning System (GPS) typically cannot penetrate the overhead forest canopy. Thus, for independent and real-time operations, vehicles must be able to perform GPS-denied flights using onboard sensing, estimation, and planning. Secondly, a collaborative mapping system would require a map fusion procedure that accurately detects overlaps between individual maps and fuses these maps into a globally consistent model of the environment. In the forests, however, correctly matching multiple overlapping maps is a challenging problem due to severe perceptual aliasing caused by the visual similarities of trees. Lastly, communication constitutes another prerequisite for collaborative exploration and mapping. However, in forest search and rescue scenarios, communication is typically unreliable and intermittent due to signal attenuation and limited transmission range.

In this work, we present a multi-UAV system for efficient exploration in large-scale unknown forest environments. Our vehicles are equipped with onboard autonomy that efficiently performs autonomous sensing, vehicle state estimation, local mapping, and exploration planning. When communication is

available, map fusion is achieved by performing collaborative simultaneous localization and mapping (CSLAM) at a central ground station. We overcome the challenge of limited communication bandwidth by leveraging *two different map representations*: a dense 3D volumetric grid representation for onboard trajectory planning, and a compact *tree-based* representation for lightweight communication with the ground station during CSLAM.

Our onboard sensing, estimation, and mapping modules are based on a 2D LIDAR sensor, where laser scans are aligned frame-to-frame for incremental vehicle pose update, collected into a 3D occupancy grid for trajectory planning, and compressed into a tree-based map for lightweight communication. We adopt a submap-based grid representation (Leonard and Feder 2001), i.e., a collection of locally segmented grid maps as opposed to a single occupancy grid, which allows the origin of each submap in the world to be optimized to correct for onboard estimation drifts after loop closure. Our submapping approach also bounds the area that is updated after incorporating each new scan, but unlike the sliding-window mapping approach, e.g. by Schmuck and Chli (2018), all previous submaps are stored and used by a dynamics-aware frontier-based planner during exploration. While dense local submaps are useful for onboard planning processes, naïve transmission of rich geometric occupancy information poses high bandwidth requirements.

¹Massachusetts Institute of Technology, Cambridge, MA, USA

²NASA Langley Research Center, Hampton, Virginia, USA

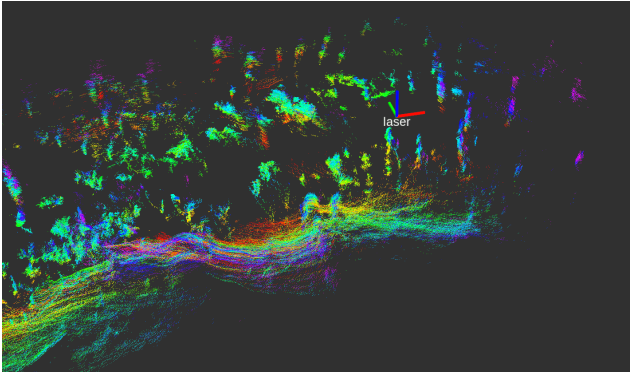
Corresponding author:

Yulun Tian

Email: yulun@mit.edu



(a) Image of one of our UAVs during a collaborative mapping mission in a forest.



(b) Raw point cloud collected by onboard laser scanner. Each individual point is colored according to its height from the ground. The vehicle pose estimated by the onboard EKF is represented as the *laser* coordinate frame.

Figure 1. Autonomous flight of one of our UAVs in a forested area within NASA Langley Research Center (LaRC). A complete video of two UAVs autonomously exploring and collaboratively mapping the forest is available at: <https://groups.csail.mit.edu/rrg/videos/iser2018>.

For lightweight communication, we compress local maps into object-based maps by detecting tree stems in each laser scan.

On the ground station, we perform CSLAM to jointly optimize all submap origins, which determine how each submap should be positioned in the world frame, as well as tree positions in the fused map. To do so, we first detect overlaps across individual submaps by performing loop closure detection. Instead of directly matching individual trees, which is prone to error due to their visual similarities, we match groups of trees using their relative positions and orientations as a unique signature. To gain additional robustness against perceptual aliasing, we include a novel stage during our data association process that jointly optimizes the set of all pairwise matches based on the criterion of *cycle consistency* (Aragues et al. 2011). Based on the final tree-to-tree correspondences between submaps, we perform landmark SLAM that jointly optimizes all submap origins and tree positions in the global map. This global map may then be inspected by the human operators at the ground station, and transmitted back to the vehicles to correct estimation drifts during onboard state estimation and mapping.

We demonstrate the proposed system in a small forest at NASA Langley Research Center (LaRC), where a team of two UAVs are each assigned a search region to completely explore (Figure 1). We show that the proposed loop

closure detection and data association algorithms result in improved precision and recall when evaluated on datasets collected at the NASA LaRC forest. Using a high fidelity simulation environment, we also show that our dynamics-aware exploration planner outperforms the classical frontier-based planner in efficiently covering the search area, and that our SLAM pipeline effectively corrects onboard estimation drifts. These experimental results show promising progress towards the practical use of multi-UAV systems for search and rescue under the forest canopy.

An early version of this work was presented at ISER 2018 (International Symposium on Experimental Robotics) (Tian et al. 2018). This paper extends our previous work with the following contributions:

1. Extension to a *deformable* submap-based representation for local mapping, which allows for correction of local estimation drifts (Section 4.1).
2. Novel use of *cycle consistent multiway matching* during centralized data association for CSLAM (Section 5.3).
3. Additional experimental results that demonstrate the usefulness of the proposed multi-UAV exploration and mapping system (Section 6 and 7).

1.1. Outline

The rest of the sections are organized as follows. We first review previous work in Section 2 and give an overview of the proposed system in Section 3. We describe in detail the onboard autonomy in Section 4 and the offboard CSLAM pipeline in Section 5. We present simulation and real flight experiments and analyze the results in Sections 6 and 7. Finally, we share main experimental insights learned and suggest future work in Section 8.

2. Related Work

2.1. Multi-Robot Mapping and Exploration

Multi-robot localization and mapping has been an active field of research. For a comprehensive survey, see also Saeedi et al. (2016); Choudhary et al. (2017); Schmuck and Chli (2018) and the references therein. Forster et al. (2013) are among the first to propose a centralized collaborative SLAM system for multiple UAVs. Each UAV runs visual odometry onboard and relays its keyframes and relative pose estimates to a ground station. The ground station detects loop closures among local maps and performs map fusion when necessary. Schmuck and Chli (2018) extend this framework by sending optimized keyframes and map points back to the vehicles to improve accuracy of local mapping.

On the other hand, Dong et al. (2015), Morrison et al. (2016) and Schuster et al. (2019) propose to run full SLAM onboard each vehicle. The incurred computation costs are further reduced in *distributed* architectures, where each robot only optimizes its local map and shares the compressed map or boundary poses with each other, see Cunningham et al. (2013); Choudhary et al. (2017); Cieslewski et al. (2018).

While distributed systems have better scalability compared to centralized ones, they do not leverage the opportunity to transfer expensive onboard operations to the ground station which has more computational power and is not limited by resource constraints. Furthermore, for search and rescue, a

fused map ultimately has to be created on the ground station and presented to the first responders. For these reasons, in this work we choose to implement a centralized architecture similar to the ones presented in Forster et al. (2013); Schmuck and Chli (2018).

The problems of search and exploration have been well-studied in the literature. Standard approaches include nearest frontier selection (Yamauchi et al. 1998), next-best-view (NBV) (Gonzalez-Baos and Latombe 2002; Bircher et al. 2016), greedy or receding horizon information gain (Feder et al. 1999; Bourgault et al. 2002), or a mixture of these methods (Charrow et al. 2015). More recently, there have been results on exploring to find hidden objects in indoor environments (Aydemir et al. 2011). For rapid exploration using a UAV, Cieslewski et al. (2017) propose to select frontiers that are reachable with minimum change in velocity.

Multi-robot exploration has also gained considerable attention over the years. Cesare et al. (2015) demonstrate a frontier-based exploration algorithm for multiple UAVs in an indoor environment. Other related work for multi-robot exploration focuses on deriving algorithms with provable performance guarantees (Singh et al. 2009; Corah and Michael 2017) and improving communication efficiency (Jensen 2018; Corah et al. 2019).

2.2. Multi-Robot Loop Closure and Data Association

Robust loop closure detection and data association form the backbone of any CSLAM system. Existing approaches for multi-robot loop closure and data association can be categorized into *pairwise* and *multiway* techniques.

2.2.1. Pairwise Methods Detecting correspondences between two sets of feature points is a well-studied problem in robotics. Classical *geometry-based* methods such as Nearest Neighbor, Maximum Likelihood, and Joint Compatibility Branch and Bound (JCBB) associate pairs of landmarks based on their Euclidean or Mahalanobis distances in a common reference frame (Neira and Tardos 2001; Zhou and Roumeliotis 2006; Kaess and Dellaert 2009; Gil et al. 2010). When a common reference frame is not available, methods based on local geometric features (Cunningham et al. 2012), Generalized Hough Transform (Paz et al. 2005), or Maximum Common Subgraph (MCS) (Bailey et al. 2000) can be used instead. Many of the above techniques can be combined with RANSAC (Fischler and Bolles 1981) for enhanced robustness.

Recently, *appearance-based* methods have shown great success in large scale place recognition (Paul and Newman 2010; Cummins and Newman 2011) and distributed visual SLAM (Cieslewski et al. 2018). Many of these methods start by detecting local features from input images or laser scans. Each feature point is typically associated with a descriptor. For visual data, popular descriptors include SIFT (Lowe 2004), SURF (Bay et al. 2006), BRIEF (Calonder et al. 2010), and ORB (Rublee et al. 2011). For laser-range data, similar descriptors have been developed which include Gestalt (Bosse and Zlot 2009), FPFH (Rusu et al. 2009), and FLIRT (Tipaldi and Arras 2010).

Although feature extraction is very fast, the number of features needed for tracking and loop closure detection

may still pose a challenge for real-time computation and communication. To address this issue, recent works begin to use more lightweight representations based on *semantic* and *object-level* models. Choudhary et al. (2017) use objects detected by convolutional neural networks (CNN) during distributed pose graph optimization. Dubé et al. (2018) represent objects with segments in 3D point clouds and use data-driven descriptors for loop closure detection.

In the forest environment, prior works have recognized trees as the distinctive objects that can aid localization and mapping (Asmar et al. 2006; Öhman et al. 2008; Tang et al. 2015; Kukko et al. 2017). The present work also uses trees as landmarks in the map representation. However, unlike prior works that consider passive SLAM with a single robot, we focus on the more general scenario of collaborative SLAM during multi-robot autonomous exploration.

In addition, state-of-the-art SLAM systems often implement a place recognition module that aggregates local features into a global descriptor for fast detection of potential loop closures. For images, notable examples include bag of visual words (Gálvez-López and Tardos 2012), vector of locally aggregated descriptors (VLAD) (Jégou et al. 2010), Fisher vectors (Jégou et al. 2012; Perronnin et al. 2010), and deep learning based methods such as NetVLAD (Arandjelović et al. 2016). For laser scans, Himstedt et al. (2014) develop the Geometric LANDmark RELations (GLARE) signature, which is later extended by Kallasi and Rizzini (2016) to be rotationally invariant in GLAROT. Note that comparing global descriptors only yields a set of candidate matches. State-of-the-art SLAM systems still employ a *geometric verification* step to validate the proposed associations; see e.g., Mur-Artal and Tardós (2017).

2.2.2. Multiway Methods For robust data association in robotics, multiway association that simultaneously considers multiple noisy pairwise associations is often used. One prominent example is the problem of rejecting outlier loop closures in pose graph SLAM (Indelman et al. 2014; Dong et al. 2015; Mangelson et al. 2018). Among the different ways of performing multiway association, a family of techniques closely related to our work attempts to achieve *cycle consistent* multi-robot data associations (Aragues et al. 2011; Montijano et al. 2013). Specifically, these works seek to resolve inconsistencies in the data associations; for example, such inconsistencies can appear when a chain of spurious pairwise associations matches two landmarks observed by the same robot. Aragues et al. (2011) propose a heuristic based on cycle detection to detect and resolve these inconsistencies.

Similarly in the computer vision community, cycle consistency has also gained considerable attention due to popular applications such as multi-shape matching (Nguyen et al. 2011; Huang and Guibas 2013) and multi-image matching (Zhou et al. 2015; Leonardos et al. 2017). Principled approaches based on spectral relaxation (Pachauri et al. 2013), semidefinite relaxation (Chen et al. 2014), distributed consensus (Leonardos et al. 2017), and spectral clustering (Fathian et al. 2019) have been proposed for solving this problem, and performance guarantees for exact matching are proved under certain noise models (Pachauri et al. 2013; Chen et al. 2014). In this work, we leverage these recent advances

to achieve cycle consistent data associations in our robust collaborative SLAM.

3. Overview

To enable independent exploration of large-scale GPS-denied forest environments, we equip each of our UAVs with an onboard autonomy module that performs autonomous sensing, vehicle state estimation, local mapping, and exploration planning; see Figure 2a. We adopt a filtering-based approach to infer the vehicle state, while merging incoming laser scans into an occupancy grid for real-time obstacle avoidance and exploration planning. When communication is available, each vehicle also transmits its local observations to a central ground station to contribute to the collaborative mapping process. To cope with the limited communication bandwidth, these local observations are first compressed into lightweight submaps consisting only of detected tree objects in the environment. A detailed description of each component of the onboard autonomy module is provided in Section 4.

The ground station performs CSLAM which fuses noisy measurements (in the form of tree-based submaps) from different vehicles into a globally consistent map of the world. This is achieved via a two stage process that consists of (i) *global data association*, which recovers the underlying correspondences between trees observed across multiple submaps and possibly by different vehicles, and (ii) *landmark SLAM*, which jointly optimizes all submap origins and tree positions in the global map. See Figure 2b for the corresponding system diagram. The optimized submap origins are transmitted back to the vehicles to correct estimation drifts during local mapping. We note that the offboard CSLAM can happen in parallel to the onboard autonomous operations of each vehicle. This centralized architecture provides sufficient tolerance against network failures which in our architecture would only delay potential map fusion, but will not hinder real-time onboard operations. We describe the centralized CSLAM pipeline in detail in Section 5.

4. Onboard Autonomy

Each of our vehicles achieves full onboard autonomy by estimating the vehicle pose in real-time and simultaneously optimizing over a local geometric map for obstacle avoidance and exploration planning. The rest of this section is organized as follows. We first describe our approach for laser-based vehicle pose estimation and 3D occupancy grid mapping (Section 4.1). We then describe our frontier-based exploration planning algorithm (Section 4.2), and lastly our object-based map compression scheme suitable for low-bandwidth communication in the forest (Section 4.3).

4.1. State Estimation and Local Mapping

Forests are challenging environments for lightweight onboard sensing. Vision-based sensors, such as RGB cameras that provide rich information about the environment, suffer from occlusions between trees, large lighting changes with movements of foliage in the wind, visual similarities between trees, and limited field of views.

Following Giamou et al. (2017), we instead adopt a 2D Hokuyo LIDAR as our main onboard sensor as it provides

a large field of view (270°), accurate depth information, and robustness to visual aliasing and lighting changes, and is also lightweight enough to be carried by a smaller UAV. In addition to the LIDAR, we also utilize a single-point downward-facing laser altimeter and an inertial measurement unit (IMU), both of which provide additional information about vehicle state.

We combine the raw measurements produced by the suite of onboard sensors in a laser-based Extended Kalman Filter (EKF) (Bachrach et al. 2011) that estimates the 6 degrees-of-freedom pose of the vehicle. We first estimate the incremental motion between two consecutive laser scans using the iterative closest point (ICP) algorithm, and subsequently fuse this estimate with height measurements from the laser-based altimeter and inertial measurements produced by the IMU.

Each vehicle uses the real-time state estimates from EKF to build a map of the explored region. In our previous work (Tian et al. 2018), each onboard map was a 3D occupancy grid produced using Octomap (Hornung et al. 2013). While occupancy grid is a popular map representation especially for the purpose of path planning, one of its drawbacks is that it is not easily amenable to correction of previous mapping errors. In our case, such corrections are often needed to account for onboard estimation drifts, which is important for the vehicle to have a more accurate understanding of the environment (e.g., in terms of explored and unknown space) and adjust its decision intelligently to maximize search efficiency.

In this work, we extend our onboard map representation to a *submap-based* representation (Leonard and Feder 2001). Each onboard map is stored as a collection of smaller 3D occupancy grids. This approach makes the onboard map *deformable*: while each submap is locally rigid, the relative transformations between submaps can be optimized using the refined pose estimates provided by CSLAM. This allows us to correct the errors accumulated during onboard vehicle estimation. An additional benefit is that at any time, the vehicle only needs to update its current submap which is computationally more efficient.

In our implementation, we initialize a new empty submap (Octomap) on each vehicle after a fixed amount of time.* To update the current submap, we transform each incoming laser scan from the local sensor frame to the coordinate frame of the submap. The resulting point cloud is then used to update the 3D octomap. Although each submap only provides local information of a small area, the union of submaps contains the same amount of information as a single global map. Therefore, while we only update the current submap during onboard mapping, we use the union of the submaps for onboard motion and exploration planning.

Several state-of-the-art systems, e.g., (Schmuck and Chli 2018), use a sliding window approach for local mapping to limit the onboard memory usage. However, such approach that discards old information is not suitable for our vehicles because they must keep track of all areas previously visited during exploration. In addition, we note that in practice the memory usage per vehicle is relatively small as each vehicle is tasked with exploring a reasonably bounded search region.

* Alternatively, one can initialize a new submap after the vehicle travels a fixed distance or after the estimation uncertainty of EKF grows beyond a threshold.

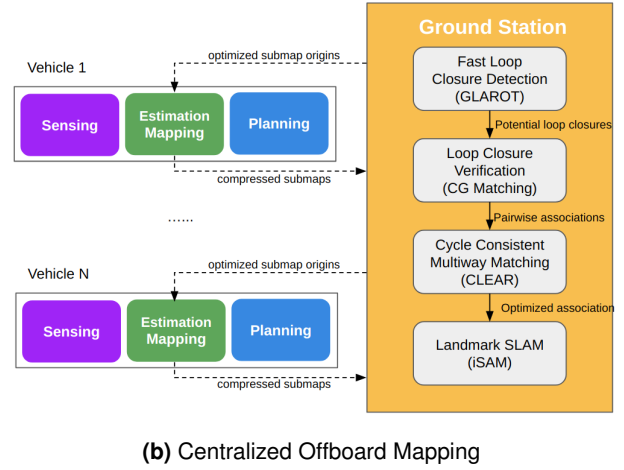
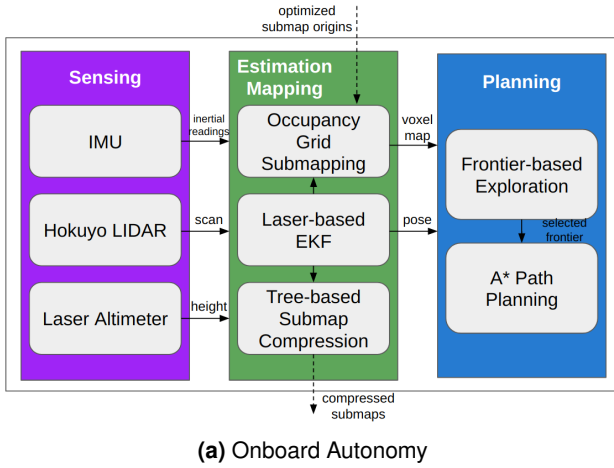


Figure 2. System architecture. Dashed lines denote communication. **(a):** Each vehicle achieves full autonomy by performing onboard sensing, vehicle state estimation, local mapping, and exploration planning. **(b):** Ground station performs CSLAM by detecting matches (loop closures) between received submaps, recovering associations between trees observed in multiple submaps, and optimize all submap origins and tree positions in the fused map.

4.2. Frontier-based Planning

We adopt a frontier-based algorithm for onboard exploration, where a *frontier* refers to a location in the current map that is on the boundary of known and unknown space. Our choice is based on the low computational cost of frontier-based algorithms compared to algorithms based on maximizing information gain. After the frontier-based planner selects the next frontier to visit, a motion planner based on A* search (Hart et al. 1968) is used on the projected 2D occupancy map to plan the optimal collision-free path for the vehicle. Exploration finishes when there are no more frontiers left in a designated search area.

While frontier-based algorithms are computationally efficient and thus more suitable for lightweight platforms, finding the best frontier for exploration using a UAV can be a challenging problem. Classic approaches usually select the closest frontier based on the Euclidean distance (Yamauchi et al. 1998). However, when using maps built with our onboard mapping system, it is often the case that the closest frontier lies directly behind the vehicle, in the blindspot of the 270° field-of-view LIDAR. Selecting these frontiers would yield rapidly changing vehicle orientations that ultimately lead to a poor mapping performance and a lack of progress towards searching uncovered ground.

In this work, we select frontiers based on a hybrid cost function that accounts for both the distance to frontiers and the vehicle dynamics, similar to the technique in (Cieslewski et al. 2017). We define the cost associated to a frontier a as

$$J(a) = J_\theta(a) + \lambda J_t(a), \quad (1)$$

where $J_t(\cdot)$ is the classic Euclidean distance of a , $J_\theta(\cdot)$ is the change in orientation required to reach a from the vehicle's current heading, and λ is a balance parameter that trades off the two cost terms. Directly incorporating the orientation change in the cost function discourages the vehicle from excessive turning and hence produces a smoother overall trajectory. In addition, accounting for orientation change also enables *continuous* update of the next-best frontier, i.e., at any time during flight, the planner can replace the

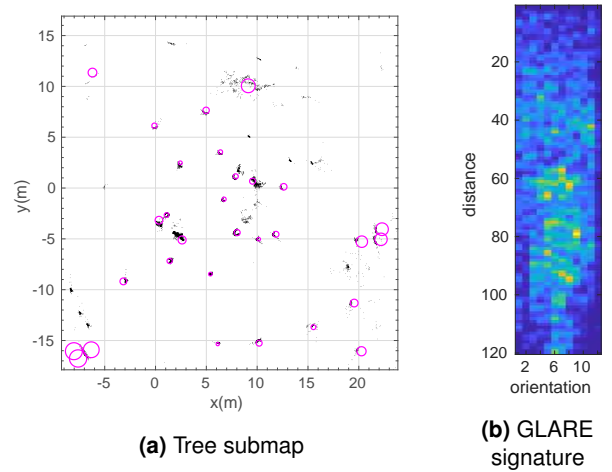


Figure 3. **(a):** Example submap generated from real forest data collected at NASA LaRC. Black dots show the raw laser returns over a period of 20 seconds. Each magenta circle shows a tree tracked within this submap, where the radius corresponds to the estimated tree stem radius. **(b):** The corresponding GLARE signature. Horizontal and vertical axes show discretizations with respect to orientation and distance, respectively. Lighter color denotes higher value.

currently selected frontier with a new frontier whose cost is significantly lower. Because of the orientation cost term $J_\theta(\cdot)$, switching to the new frontier typically produces minimal heading changes and thus encourages safe flight behavior. In contrast, a dynamics-agnostic planner, e.g., with a purely distance-based cost, has to wait until the vehicle reaches the current frontier to be able to select the next frontier, which is not time efficient.

4.3. Tree-based Map Compression

While dense volumetric maps provide accurate geometric information for path planning, they are not data efficient and hence are not suitable for communication over a low-bandwidth wireless network. Other representations such as

3D point clouds (Schuster et al. 2019) or feature-based maps (Schmuck and Chli 2018) can be more lightweight, but both can still result in potentially heavy data payload.

To achieve lightweight communication, we turn to *object-based* representations, more specifically a *tree-based* representation (Kukko et al. 2017). Before transmission, we compress each submap into a sparse collection of trees as shown in Figure 3a. This is done by first clustering beams in each LIDAR scan using Dirichlet process clustering (DP-means) (Campbell et al. 2013). Each cluster of points is then fitted to a circle in 2D that represents a tree trunk, by applying an algebraic fitting algorithm (Taubin 1991) that estimates a tree position and radius and returns a residual error. If the initial residual error after the algebraic fitting is sufficiently low, a geometric fitting process based on Levenberg-Marquardt (Chernov 2010) that uses the algebraic fitting as initial guess is employed to refine the estimated tree parameters. A tree detection is accepted if the final residual error after geometric fitting is less than 0.015, the tree has a radius greater than 0.1 m, and the observed LIDAR beams cover more than 30% of the tree trunk.

For improved stability, we also perform tree tracking and culling within each submap. At every time step, a newly detected tree is combined with the closest previously detected tree in the same submap if their estimated positions are within 0.5 m and their radii differ less than 10%. If the above two conditions hold, the observation count of the original tree is incremented by one; if not, a new tree is initialized in the current submap using parameters of the newly detected tree. Before transmitting to the ground station, we optionally perform culling inside the submap, by removing trees with observation counts less than a threshold τ_{cull} . Here, τ_{cull} is a tunable parameter designed to cope with varying level of noise during tree detection.

5. Offboard Collaborative SLAM

On the ground station, we construct a globally consistent map of the world by fusing identical trees detected across multiple submaps and performing landmark SLAM over the fused trees. The overall problem is combinatorial in nature and thus difficult to solve optimally; however, practical applications, e.g., search and rescue, often require a solution that is efficient and, ideally, real-time. In order to meet such performance demand, we make use of the following centralized pipeline to efficiently (albeit approximately) solve the global mapping problem on the ground station; see Figure 2b. First, we identify potential matches between pairs of submaps, i.e., potential loop closures, using a compact descriptor developed for 2D point landmarks (Section 5.1). We then verify each potential match by solving for the pairwise correspondences between trees in the two submaps (Section 5.2). Finally, the set of all pairwise associations are verified based on cycle consistency (Section 5.3) to overcome perceptual aliasing. Given the final data association results, we perform landmark SLAM to jointly optimize all submap origins and tree positions in the global map (Section 5.4).

5.1. Fast Loop Closure Candidate Detection

To efficiently detect potential loop closures between pairs of submaps, we build a GLARE (Himstedt et al. 2014)

descriptor for each received submap on the ground station. GLARE is an efficient method for encoding relative landmark (i.e. tree) positions in a single map. For every pair of trees (i, j) , we compute their distance $\rho_{i,j}$ and absolute relative angle $\theta_{i,j}^+$. We then assign these values to bins in a 2D histogram $(\theta_{i,j}^+, \rho_{i,j}^t) \in \text{bin}(n_\theta, n_\rho)$, where $n_\theta \in \{1, 2, \dots, N_\theta\}$ and $n_\rho \in \{1, 2, \dots, N_\rho\}$ are indices corresponding to the quantization of $(\theta_{i,j}^+, \rho_{i,j}^t)$ in the range $[0, \rho_{\text{max}}] \text{m} \times [0, \pi] \text{rad}$. To account for noise during tree detection, we apply a Gaussian blur to the histogram of each feature pair. The GLARE descriptor is computed as the sum of the 2D histograms over all pairs. Following Giamou et al. (2017), we set the default histogram resolutions to be $N_\rho = 120, N_\theta = 12$. Figure 3b shows the GLARE signature corresponding to the submap in Figure 3a.

To determine if two submaps are likely to be a loop closure, we compare their GLARE descriptors using the GLAROT procedure proposed by Kallasi and Rizzini (2016). GLAROT provides a rotation-invariant distance metric, by computing the *shifted L_1 distance* between two GLARE descriptors $G^s, G^t \in \mathbb{R}^{N_\rho \times N_\theta}$,

$$SL_1(G^s, G^t) = \min_{0 \leq k < N_\theta} \sum_{i=0}^{N_\rho-1} \sum_{j=0}^{N_\theta-1} |G_{i,j}^t - G_{i,(j+k) \bmod N_\theta}^s|. \quad (2)$$

Each GLAROT query requires $N_\rho \times N_\theta^2$ operations which is very fast on standard CPUs. A pair of submaps (M^s, M^t) is declared to be a loop closure candidate, if their GLAROT distance $SL_1(G^s, G^t)$ is below a threshold ϵ_{GLAROT} . This process serves as an efficient filtering step that reduces the search space for loop closures to a small set of candidate matches. To verify if each candidate is a true loop closure, we apply a pairwise data association procedure which identifies the tree-to-tree correspondences between the two submaps.

5.2. Loop Closure Verification

For each potential loop closure between a pair of submaps (M^s, M^t) , we verify if (M^s, M^t) forms a true loop closure by solving an element-wise data association problem that returns the correspondences between trees in the two submaps. Note that as M^s and M^t could potentially come from different vehicles, classical pairwise association methods such as Nearest Neighbor or JCBB which rely on a common reference frame could not be used. Instead, we perform correspondence graph (CG) matching (Bailey et al. 2000), which is observed to work better compared to alternative methods based on the Generalized Hough Transform or RANSAC (Giamou et al. 2017). Let $\{o_i^s\}$ and $\{o_j^t\}$ represent the set of objects in M^s and M^t . In addition, let $\{p_i^s\}, \{p_j^t\}$ be the positions of these objects in the coordinate frames of M^s and M^t , respectively. A correspondence graph is an undirected graph in which each vertex $u_{i,j}^{s,t}$ denotes a hypothetical match between $o_i^s \in M^s$ and $o_j^t \in M^t$. Two vertices $u_{i,j}^{s,t}, u_{k,l}^{s,t}$ are connected by an edge if relative transformation is preserved, i.e., if,

$$\|(p_i^s - p_k^s) - (p_j^t - p_l^t)\|_2 \leq \epsilon_{\text{CG}}, \quad (3)$$

where ϵ_{CG} is an adjustable tolerance parameter.

Given the correspondence graph, we find the maximal set of pairwise compatible correspondences between M^s and M^t by

finding the maximum clique. The resulting data association can be written as a partial permutation $\tilde{\pi}_t^s$ which maps a subset of objects in M^s to M^t . We use the tilde notation as a reminder that $\tilde{\pi}_t^s$ could still contain wrong associations, e.g., due to strong perceptual aliasing in the forest. For numerical computations in the next section, each $\tilde{\pi}_t^s$ is also represented as a partial permutation matrix $\tilde{\Pi}_t^s \in \{0, 1\}^{m^s \times m^t}$, where

$$\tilde{\Pi}_t^s(i, j) = \begin{cases} 1, & \text{if } \tilde{\pi}_t^s(i) = j, \\ 0, & \text{otherwise,} \end{cases} \quad (4)$$

and m^s and m^t are the sizes of the two submaps. M^s and M^t are declared to be a loop closure, if $\tilde{\pi}_t^s$ contains sufficient amount of matches, specified by a tunable parameter τ_{cg} .

We make a note on the complexity of CG matching. Although the maximum clique problem is combinatorial in nature, our object-based representation allows us to solve it efficiently and in real time. To solve the maximum clique problem, we use the implementation provided by Konc and Janei (2007). Empirical runtime results are reported in Section 7.

5.3. Globally Consistent Loop Closures

Given a collection of noisy pairwise associations $\{\tilde{\pi}_t^s\}$ between n submaps, we perform a final optimization to recover the *global* association $\{\pi_u^s\}$, which maps objects in each submap M^s to the *universe* U of objects, i.e., the set of all trees in the forest. Recovering $\{\pi_u^s\}$ requires the pairwise associations $\{\tilde{\pi}_t^s\}$ to be *cycle consistent*, i.e., the composition of pairwise mappings along any cycle of submaps should result in the identity mapping (Nguyen et al. 2011).

To better understand the importance of cycle consistency, we look at the *data association graph* \mathcal{G} (Leonardos et al. 2017) induced by $\{\tilde{\pi}_t^s\}$.[†] With a slight abuse of notation, we let each vertex in \mathcal{G} represent an object o_i^s in a submap M^s . Two vertices o_i^s, o_j^t are connected by an edge if they are matched in the input associations, i.e., if $\tilde{\pi}_t^s(i) = j$. We note that these edges are inherently *transitive*: if o_i^s is matched to o_j^t and o_j^t is matched to o_k^t , then it must be true that o_i^s is matched to o_k^t . Tron et al. (2017) show that $\{\tilde{\pi}_t^s\}$ is cycle consistent if and only if the corresponding data association graph consists of disjoint cliques, and furthermore no two objects from the same submap appear in the same clique. In this case, map fusion happens naturally by assigning each clique in \mathcal{G} to a unique object in the universe U . Figure 4a provides an example.

In practice, however, $\{\tilde{\pi}_t^s\}$ often contain noisy matches that violate the cycle consistency principle; an example is shown in Figure 4b. After invoking the transitive property of all edges, a chain of spurious associations (red edges) would incorrectly fuse two objects belonging to the same submap, which contradicts the assumption that each submap contains distinct objects. Therefore, for map fusion, we must find a cycle consistent set of pairwise associations $\{\pi_t^s\}$ that resembles the input associations $\{\tilde{\pi}_t^s\}$ as much as possible. Given $\{\tilde{\pi}_t^s\}$, it is again straightforward to recover the underlying global associations $\{\pi_u^s\}$, by assigning each clique in the induced data association graph of $\{\tilde{\pi}_t^s\}$ to a unique object. In the computer vision literature, this procedure is known as *cycle consistent multiway matching* (Pachauri et al. 2013).

Among all algorithms proposed for cycle consistent multiway matching, we choose CLEAR (Consistent Lifting, Embedding, and Alignment Rectification) proposed by Fathian et al. (2019) for its high precision and superior speed. CLEAR takes as input the aggregate matrix,

$$A = \begin{bmatrix} 0 & \tilde{\Pi}_2^1 & \cdots & \tilde{\Pi}_n^1 \\ \tilde{\Pi}_1^2 & 0 & \cdots & \tilde{\Pi}_n^2 \\ \vdots & \vdots & \ddots & \vdots \\ \tilde{\Pi}_1^n & \tilde{\Pi}_2^n & \cdots & 0 \end{bmatrix}, \quad (5)$$

which corresponds to the adjacency matrix of \mathcal{G} . Let D denote the (diagonal) degree matrix of \mathcal{G} . The Laplacian and normalized Laplacian of \mathcal{G} are defined as follows,

$$L \triangleq D - A, \quad L_{\text{nm}} \triangleq D^{-\frac{1}{2}} L D^{-\frac{1}{2}}. \quad (6)$$

From here, the algorithm proceeds in two stages. In the first stage, the number of objects m in the universe is estimated from the spectrum of the normalized Laplacian L_{nm} . In the second stage, an eigendecomposition is performed over L_{nm} to obtain an embedding vector $v_i^s \in \mathbb{R}^m$ for each vertex o_i^s in \mathcal{G} . These embeddings are then used to cluster vertices into m disjoint cliques using the Hungarian algorithm.

The final global data association $\{\pi_u^s\}$ is obtained by assigning vertices in each clique to a unique object in the universe, i.e., $\pi_u^s(i) = c$ if vertex o_i^s belongs to clique c . In addition, π_u^s can also be used to recover a cycle consistent pairwise matching simply via,

$$\pi_t^s = \pi_u^s \circ \pi_t^u, \quad (7)$$

where \circ denotes the composition operator for permutations. Further details can be found in Fathian et al. (2019).

5.4. Global Landmark SLAM

After solving for the global data association $\{\pi_u^s\}$, we perform SLAM to refine the estimates of all poses and objects in the fused map. To do this, we jointly optimize over the origin $x_t \in \text{SE}(2)$ of each submap M^t , which also corresponds to the vehicle pose when M^t is initialized, as well as the positions of the m objects $l_1, \dots, l_m \in \mathbb{R}^2$ in the environment. Recall that m is estimated by CLEAR; see Section 5.3.

Following the standard formulation of landmark SLAM, we consider two types of measurements during optimization. First, we use *odometry* measurements $z_{t+1}^t \in \text{SE}(2)$ extracted from EKF, which links consecutive submaps belonging to the same vehicle. For two submaps from different vehicles, an odometry measurement is not available as these vehicles do not share a common coordinate system. Second, we also consider *observation* measurements which links a map origin to landmarks observed in this submap. These measurements can be extracted from the global data association $\{\pi_u^s\}$: for each object o_i^s in map M^s , we retrieve the index c of the corresponding tree via $c = \pi_u^s(i)$. An observation is then created between x_s and l_c , with a relative transformation constraint specified by $p_i^s \in \mathbb{R}^2$, where p_i^s is the observed position of this tree in the coordinate frame of map M^s .

[†] \mathcal{G} should be distinguished from the correspondence graph defined in the previous section for pairwise association.

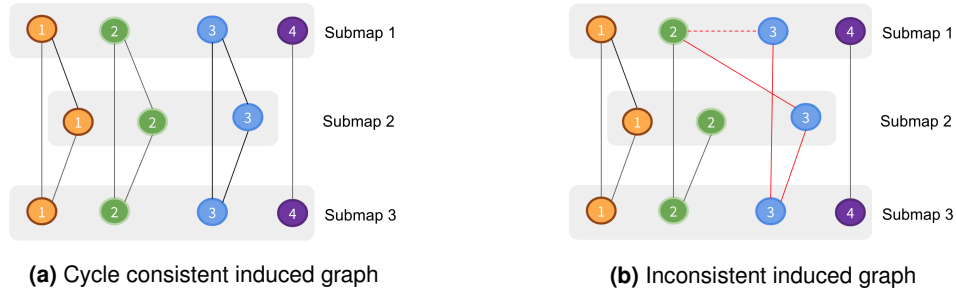


Figure 4. Example data association graphs. Each vertex (circle) represents an object (tree) in a submap. Two vertices are connected if the corresponding objects are matched in the input pairwise associations. **(a):** If the input associations are cycle consistent, objects matched together will form disjoint cliques. In this case, it is straightforward to read out the global data association by assigning each clique to an object in the universe. **(b):** In practice, a chain of spurious associations (red edges) might violate cycle consistency and incorrectly fuse two objects in the same submap (red dashed edge). We remove such noisy associations based on cycle consistency.

After all variables and measurements are initialized, we use iSAM (Kaess et al. 2008) to carry out the nonlinear optimization. Finally, the optimized map origins $\{x_t\}$ are transmitted back to the vehicles to correct estimation drifts during local estimation, by realigning all onboard submaps using the updated estimates of $\{x_t\}$.

6. Simulation Experiments

In order to evaluate the performance of the proposed exploration and SLAM algorithms over many trials, we leveraged a high fidelity simulation environment, and used largely the same set of parameters as in the following real-world experiments. Certain parameters were different to compensate for the differences in the simulation and the real world, e.g., the limit on maximum acceleration was set much higher in real-world experiments to compensate for unmodeled external forces such as wind.

6.1. Simulation Setup

Vehicle dynamics and IMU readings for a simulated vehicle were generated using the Drake toolbox (Tadrake 2014) and a quadrotor model as described in (Mellinger et al. 2012). To test integration with the full stack, we also utilized the Pixhawk (Meier et al. 2012) Software-In-The-Loop (SITL) to simulate the motor commands from the Pixhawk, which were fed back into the Drake dynamics model. We used the Unity game engine to simulate 2D laser scans in a randomly generated forest environment at roughly 30 Hz with a 270° field of view and 30 m range. All sensor measurements were simulated with low noise. The simulated setpoints generated by the motion planner were passed to the Pixhawk SITL.

6.2. Exploration Results in Simulation

We evaluated the proposed frontier-based exploration planner in simulation. A single UAV was tasked with covering a 20m × 20m search area in a randomly generated forest. To benchmark our proposed planner, we also implemented the classical frontier selection algorithm that greedily selected the closest frontier in terms of the Euclidean distance (Yamauchi et al. 1998). For comprehensive evaluation, different search areas with varying search difficulty (e.g., density of obstacles) are assigned to the vehicle. For each search area, multiple exploration missions were carried out

Table 1. Comparison with baseline planner in three different search areas in simulation. Each planner was evaluated multiple times inside each area and average completion time and flight speed were recorded. In all three cases, the proposed planner was able to maintain a higher velocity while covering the search area more efficiently, resulting in a much shorter average exploration time compared to the baseline planner.

Area	Planner	Duration (sec)	Avg. Speed (m/sec)
1	Proposed	313.50	0.84
1	Baseline	504.87	0.69
2	Proposed	340.52	0.82
2	Baseline	448.91	0.71
3	Proposed	302.41	0.80
3	Baseline	477.96	0.72

and average performances are recorded in Table 1. The proposed planner clearly outperformed the baseline planner in terms of both the total time to complete the mission and the average speed during flight. Figure 5 shows the trajectory of the proposed planner 5a-5d and the baseline planner 5e-5h in an example search area. As expected, the proposed planner produced a much smoother overall trajectory compared to the baseline and completed the mission in a shorter period of time.

6.3. SLAM Results in Simulation

We evaluated the capability of our submap-based map representation (Section 4.1) to correct onboard estimation drifts. The UAV was tasked with exploring a 20m × 20m search area in simulation, which was different from the one used in the previous section. The vehicle initialized a new submap every 5 seconds.

Figure 6a shows the ground truth trajectory (yellow) and the trajectory estimated by EKF (blue). As expected, the EKF estimates suffered from accumulated estimation drifts. To correct the drifts, we applied our SLAM pipeline described in Section 5 to optimize the origins of individual submaps, and refined the estimated trajectory based on the optimized submap origins.[‡] The resulting trajectory (red)

[‡]We did not report CSLAM results in simulation, because our simulation currently only supports single vehicle exploration. Nevertheless, when evaluating estimation accuracy, the number of vehicles is nearly irrelevant

mostly matched the ground truth, confirming the accuracy of the SLAM solution.

To provide additional quantitative results, we also recorded the evolution of the absolute trajectory error (ATE) (Sturm et al. 2012), defined as the average distance between ground truth poses and estimated poses. Due to estimation drifts, the ATE associated to EKF eventually exceeded 0.25 m; in contrast, performing SLAM effectively bounded the ATE below 0.03 m.

7. Flight Experiments

Real flight tests were performed in the forest at NASA LaRC, shown in Figure 1. To test the proposed real-time planning and CSLAM algorithms, we deployed a team of two quadrotors to perform the multi-agent mapping and coverage task. We report qualitative planning and CSLAM performance, as well as analysis of data payload size and algorithm runtimes (Section 7.2). We note that the reported real-time planning results were the same as in our previous work (Tian et al. 2018), with the frontier-based planning occurring in a single onboard map. Nevertheless, all CSLAM results were updated to incorporate the improvements (notably the submap-based representation and cycle consistency multiway matching) made in this work. Additionally, we performed extensive offline analysis on the global data association methods described in this work using the data collected by a single vehicle from the same experiment (Section 7.3).

7.1. Outdoor Flight Setup

Each vehicle was a modified DJI F450 carrying a horizontally mounted Hokuyo UTM-30LX laser rangefinder, a Pixhawk PX4 unit providing inertial measurements and motor commands, a downward-facing LidarLite for altitude measurements, and an Intel NUC computer for onboard computation. The Hokuyo produced laser measurements at a rate of 40 Hz over an angular field of view of 270° with 0.25° angular resolution. The inertial measurements and LidarLite measurements were processed at 100 Hz. The vehicles were commanded to fly at 1.8 m altitude with a maximum velocity of 2.0 m/sec, and a maximum acceleration of 0.4 m/sec^2 . Communication with the ground station was maintained via 5.8 GHz WiFi; alternatives for peer-to-peer (P2P) communication, e.g., Long Range (LoRa) radios, exist for larger search regions. A new submap was initialized on each vehicle after 5 seconds. Other parameters used during onboard and offboard operations were: $\lambda = 0.5$ (Section 4.2), $\tau_{\text{cull}} = 3$ (Section 4.3), $\epsilon_{\text{GLAROT}} = 1.5$ (Section 5.1), $\epsilon_{\text{CG}} = 0.15$ (Section 5.2), and $\tau_{\text{CG}} = 7$ (Section 5.2).

7.2. Real-time Planning and CSLAM Results

In the outdoor experiments, our vehicles were started at different locations with unknown relative positions. The mission was specified by non-overlapping search area of size $17\text{m} \times 20\text{m}$ for each vehicle. Each vehicle was tasked with observing the entire search region. Each search area was initially unknown; as the vehicles individually completed the coverage task, they established inter-trajectory loop closures based on similar configurations of trees observed during flight. The individual submaps collected during the experiment from

both vehicles were then fused real-time on the ground station. The progress of the planners throughout the flight is shown in Figure 7 and matching onboard camera images are shown in Figure 8.

Since the proposed planner preferred frontiers with smaller orientation change, we observed that the resulting flight trajectory exhibited bias towards a natural spiral pattern. Vehicle 1 completed the exploration mission after 122 seconds, with an average flight speed of 2.66 m/sec; vehicle 2 completed the mission after 135 seconds, with an average flight speed of 2.65 m/sec. Note that due to measurement noise, the calculated average speeds were higher than the maximum allowed speed (2.0 m/sec) even after applying a low-pass filter to the raw velocity measurements.

Figure 9 shows the evolution of the global object (tree) map on the ground station. For cleaner visualization, we only show tree landmarks that have been observed in at least 3 submaps. At $t = 30$ sec (Figure 9a), no inter-trajectory loop closure was detected and the two vehicle trajectories were arbitrarily aligned. The first inter-trajectory loop closure was established at $t = 45$ sec and map fusion happened subsequently (Figure 9b). Afterwards, all newly received submaps from the two vehicles were consistently fused into the global map (Figure 9c-9d). In addition, we also rendered the fused global 3D occupancy grid at $t = 120$ sec, by aligning all submaps in the world frame using their optimized origins in Octomap (Hornung et al. 2013). The resulting global map is shown in Figure 10. Note that in practice, constructing the global occupancy grid would require vehicles to transmit their full local occupancy grids which could be communication intensive. In contrast, our tree-based map representation shown in Figure 9 captures all the essential geometric information in each submap and is still lightweight enough for low-bandwidth communication.

To further demonstrate the efficiency of the proposed CSLAM framework, we also evaluated the incurred runtime and data payloads. Figure 11 shows the total runtime of GLAROT (Section 5.1), CG matching (Section 5.2), CLEAR (Section 5.3), and iSAM (Section 5.4), each as a function of the number of submaps received at the ground station. We observed that all modules demonstrated satisfactory speeds; in particular, GLAROT and iSAM were computationally very efficient and hence capable of running in real-time. In comparison, the pairwise and multiway data association steps (using CG matching and CLEAR, respectively) incurred higher computation costs. In practice, however, CG matching can be made real-time by storing and reusing previously computed matches. On the other hand, the CLEAR algorithm could also be accelerated by implementing a block singular value decomposition (SVD) method that exploits the separable structure of the underlying data association graph (Fathian et al. 2019). Still, as the number of submaps grows, we note that multiway association is likely to become the computation bottleneck of the overall system. Thus, reducing the computational cost of this step, via an incremental algorithm that can reuse previously computed results, remains an important avenue for future work.

because we can always assume the trajectories are produced by a single vehicle. Also, see Section 7.2 for real-world CSLAM results with two UAVs.

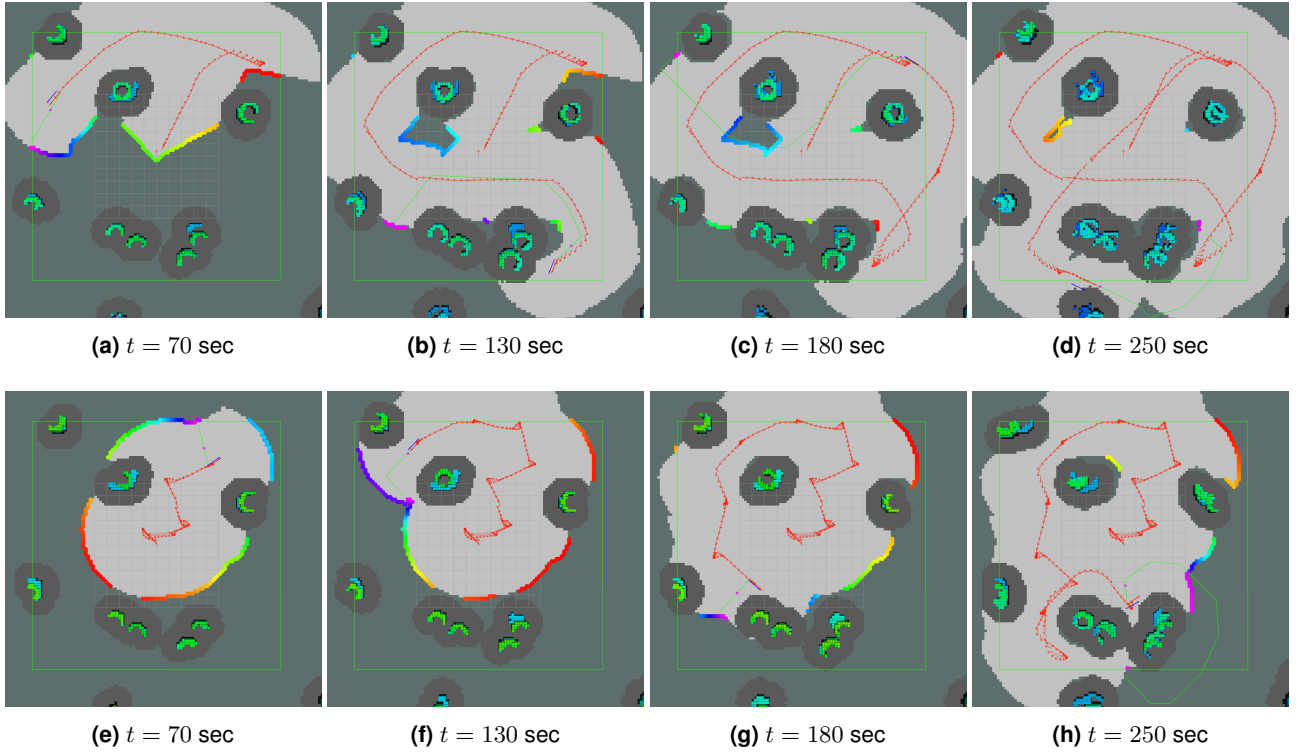
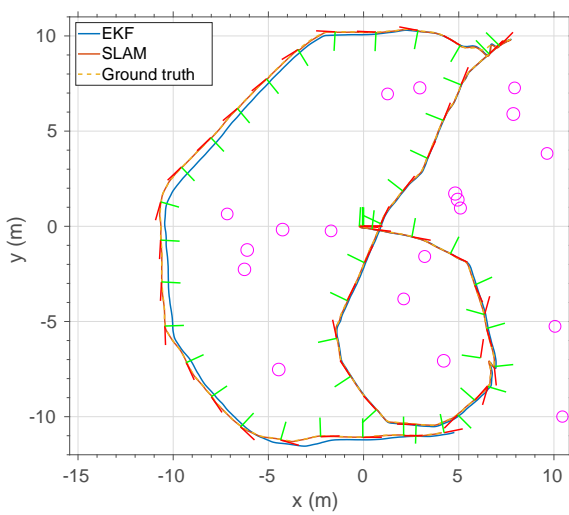
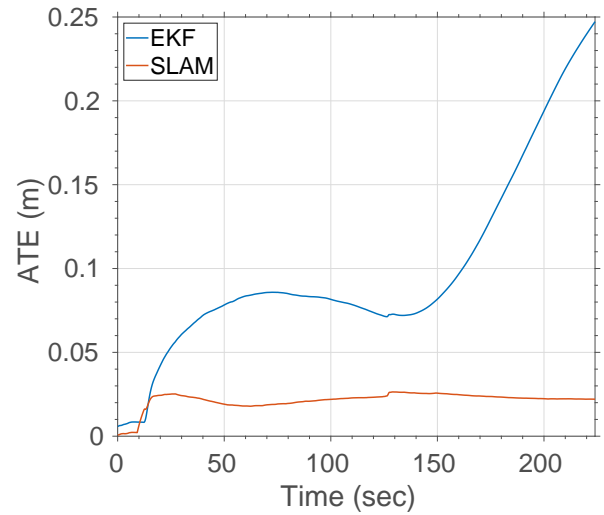


Figure 5. Vehicle trajectories and partial maps in simulation at different time steps (seconds). (a)-(d) show the proposed planner; (e)-(h) show the baseline planner. Green rectangle denotes the search area assigned to the vehicle. Colored point clouds shows the set of all frontiers with colors representing different costs (magenta to red in increasing cost). Red path shows the trajectory taken by the vehicle. The trajectory in (a)-(d) is smoother and more time-efficient compared to the trajectory in (e)-(h). At $t = 250$ sec, the proposed planner nearly completed the mission, while the search area was only partially explored by the baseline planner.



(a) Trajectory estimates in simulation



(b) Absolute trajectory error (ATE) in simulation

Figure 6. (a) Vehicle trajectory estimated by EKF (blue) and SLAM (red) in simulation. The ground truth trajectory is shown in yellow, which mostly overlaps with the SLAM estimates. Each coordinate frame shows the optimized origin of a submap. Each magenta circle represents a tree optimized during landmark SLAM. (b) Absolute trajectory errors (ATE) (Sturm et al. 2012), defined as the average distance between ground truth poses and estimated poses, as a function of exploration time. While the ATE associated to EKF exceeded 0.25 m, performing landmark SLAM bounded the ATE below 0.03 m. The results clearly demonstrate the ability of the proposed SLAM pipeline to correct onboard estimation drifts.

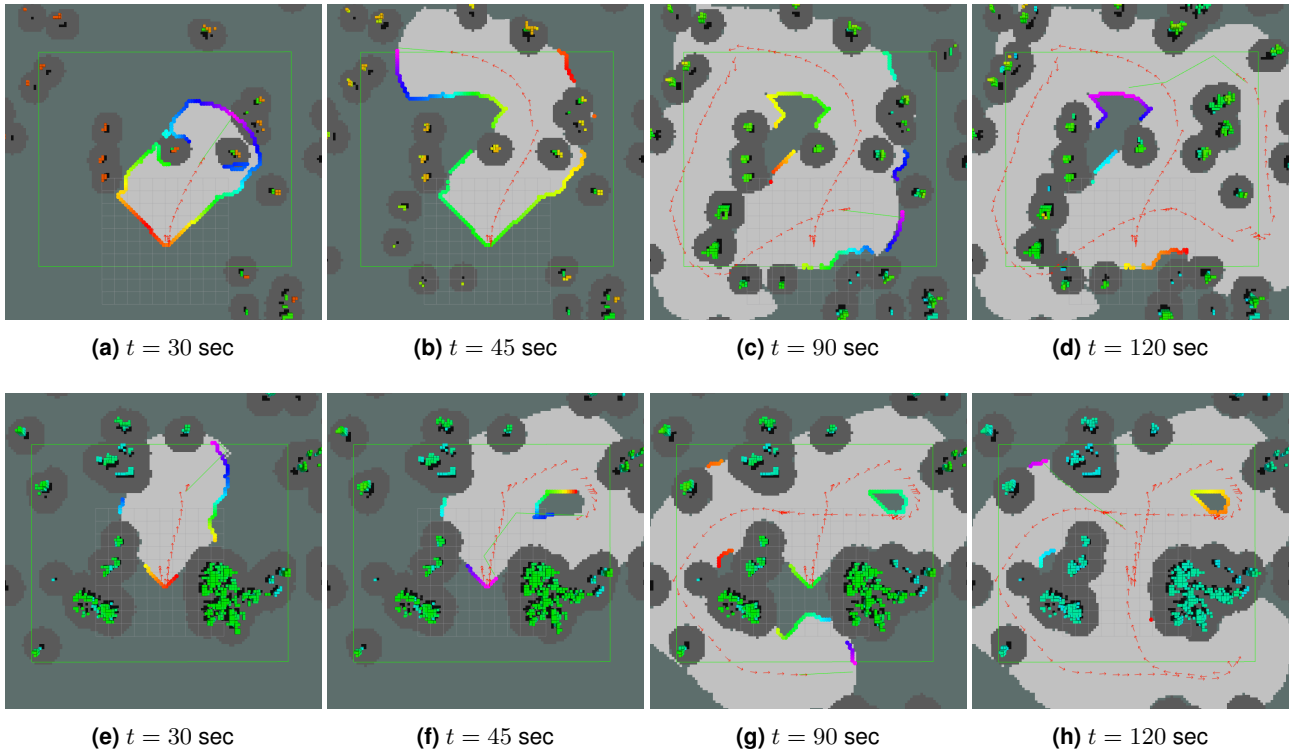


Figure 7. Vehicle trajectories and partial maps in real flight tests at different time steps (seconds). (a)-(d) show the trajectory of the first vehicle and (e)-(h) show the second vehicle. Since the proposed planner preferred frontiers with smaller orientation change, the flight trajectory exhibited bias towards a natural spiral pattern.

Finally, Figure 12 shows the total data payloads received at the ground station as a function of the number of submaps. Our calculation did not include additional communication incurred by network protocol overhead. Note that the growth in data payloads was not exactly linear with respect to the number of submaps. This is because each submap contained different number of trees depending on the specific area it covered. Overall, the proposed tree-based map representation incurred minimal communication (at most 8kB with 48 submaps) demonstrating its usefulness for low-bandwidth and real-time communication during search and rescue.

7.3. Data Association Results

Post-flight, we performed additional offline evaluations of the proposed pairwise and multiway data association algorithms (Section 5.2-5.3) using data collected by vehicle 2 (yellow trajectory in Figure 10). For this experiment, GLAROT (Section 5.1) was disabled and loop closure was attempted on every pair of submaps received at the ground station. To benchmark our methods, we also implemented the approach in (Giamou et al. 2017) which uses stabilized FLIRT features obtained from DP-means clustering. Ground truth (e.g., GPS) data was not available in our forest datasets; instead, we used estimates provided by onboard EKF to verify proposed pairwise associations. Specifically, a pair of matched trees was declared to be a true match if their positions as estimated by EKF in the world frame were sufficiently close. For short-duration flights, we expect this metric to be relatively accurate.

Figure 13 shows the resulting precision and number of correct pairwise associations (unnormalized recall)[§]. For each submap, an equal number of stabilized FLIRT features

(Giamou et al. 2017) and tree landmarks were extracted. CG matching (Section 5.2) with varying tolerance threshold ϵ_{CG} were performed to obtain the resulting data points for FLIRT and trees. For trees, we further optimized the initial pairwise associations with the CLEAR algorithm (Section 5.3). In the forest, the proposed tree detection algorithm unsurprisingly outperformed stabilized FLIRT features. Furthermore, CLEAR was able to improve both precision and recall by simultaneously rejecting false associations and suggesting more correct associations. This result demonstrates the usefulness of cycle consistent multiway association as an additional step for CSLAM.

To provide more insights on the benefits of cycle consistent multiway matching, Figure 14 shows part of the data association graph before and after optimizing with CLEAR. Each triangle represents a tree colored according to the submap it belongs to. Two trees from different submaps are connected by an edge if they are matched in the given data association. For visualization purpose, all submaps are aligned in the world frame, i.e., each object is drawn at the corresponding position estimated by EKF. Thus, objects that correspond to the same tree in the forest should appear close to each other. Due to perceptual aliasing, the initial associations from CG matching contained several wrong correspondences, shown as the long edges in Figure 14a. By jointly optimizing over all pairwise matches, CLEAR was able to reject these outliers as shown in Figure 14b. Furthermore, the resulting data association is guaranteed to be cycle consistent. This

[§] We do not show recall as the total number of correct pairwise associations in this dataset is unknown.

(a) Vehicle 1 at $t = 30$ sec(b) Vehicle 1 at $t = 45$ sec(c) Vehicle 1 at $t = 90$ sec(d) Vehicle 1 at $t = 120$ sec(e) Vehicle 2 at $t = 30$ sec(f) Vehicle 2 at $t = 45$ sec(g) Vehicle 2 at $t = 90$ sec(h) Vehicle 2 at $t = 120$ sec

Figure 8. Images from onboard GoPro camera at different time steps (seconds); (a)-(d) show images from the first vehicle and (e)-(h) show images from the second vehicle. Frames are approximately aligned with the vehicle trajectories shown in Figure 7.

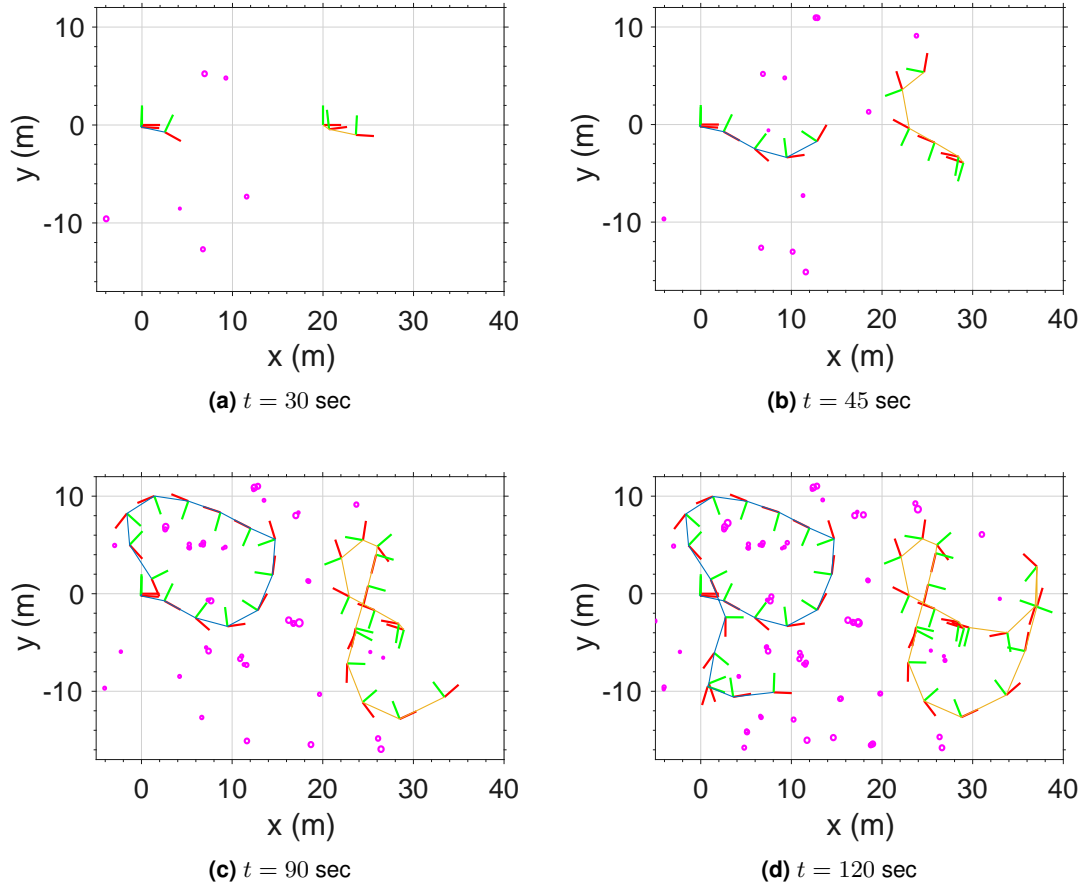


Figure 9. Global object (tree) map on the ground station. Each coordinate frame represents the origin of a submap in the world frame. Vehicle trajectories are shown as blue and yellow lines. Each magenta circle represents a tree whose position is optimized during landmark SLAM, where the radius corresponds to the estimated tree stem radius. For cleaner visualization, we only show tree landmarks that have been observed in at least 3 submaps. At $t = 30$ sec, no inter-trajectory loop closure was detected and the two vehicle trajectories are arbitrarily aligned, as shown in (a). After the first inter-trajectory loop closure was established at $t = 45$ sec, the individual submaps from the two vehicles were consistently fused into the global map as shown in (b)-(d).

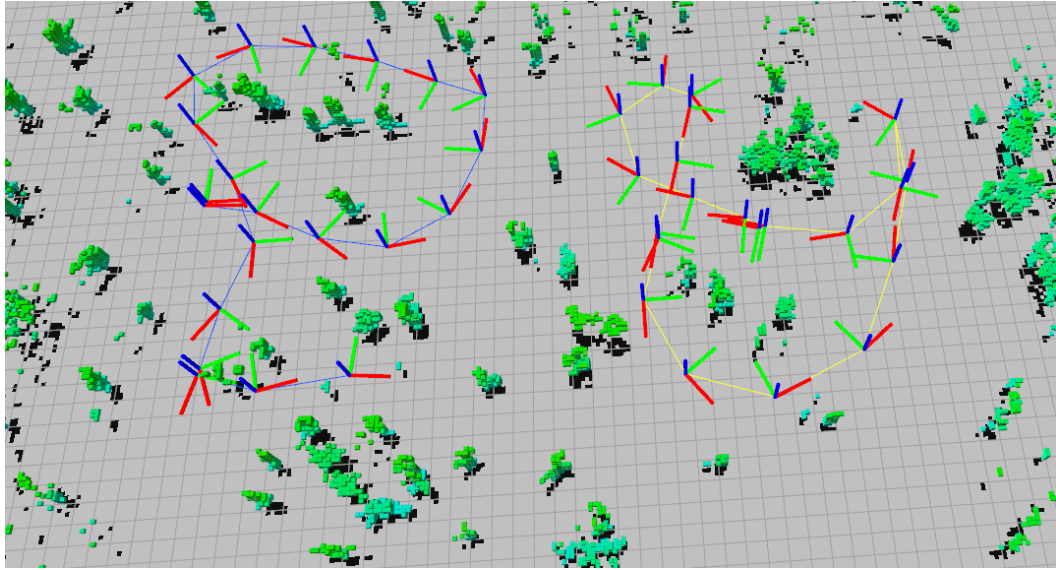


Figure 10. Fused 3D occupancy grid and vehicle trajectories at $t = 120$ sec. Each coordinate frame represents the origin of a submap in the world frame. Vehicle paths are shown in blue and yellow. The 3D map is represented as a voxel grid with an altitude-based colormap for occupied cells (blue to green in increasing altitude). In addition, we also show the projected 2D map. The cells are colored so that black denotes occupied cells, grey denotes free cells, and dark grey denotes unvisited cells (none in this figure).

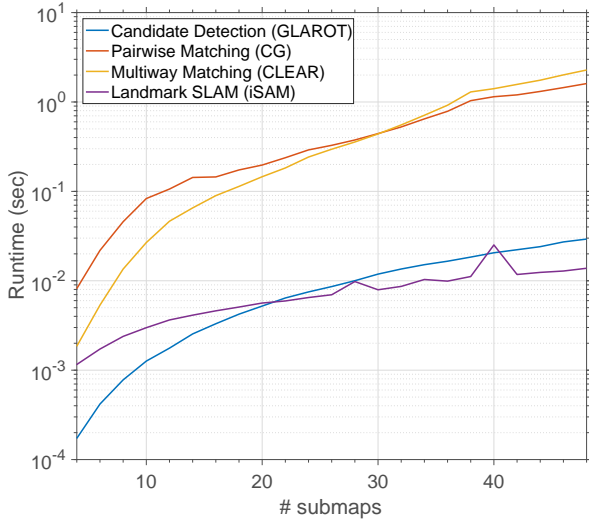


Figure 11. Total runtime of each module in the proposed CSLAM pipeline: GLAROT, CG matching, CLEAR, and iSAM, each as a function of the total number of submaps received at the ground station. All modules demonstrated satisfactory speeds. We note that CLEAR could be further accelerated by implementing the block SVD method suggested by Fathian et al. (2019).

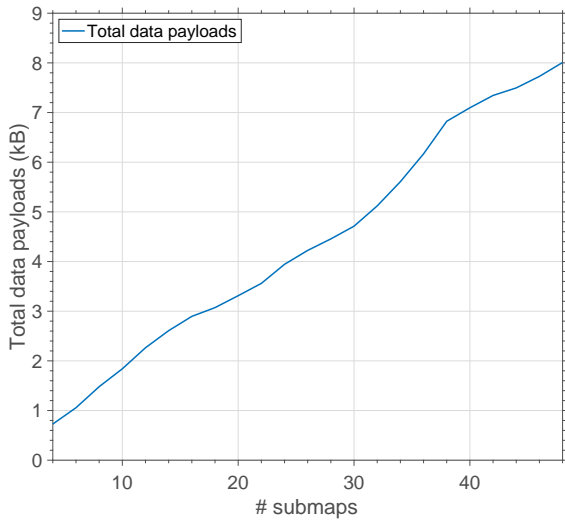


Figure 12. Data payloads, in kilobytes (kB), received at the ground station as a function of the number of submaps. Our calculation did not include additional communication incurred by network protocol overhead. In this figure, the maximum payload is 8kB corresponding to a total of 48 submaps.

means that the graph shown in Figure 14b only contains disjoint cliques which makes subsequent map fusion possible; see Section 5.3.

8. Conclusions and Future Work

We presented a collaborative exploration and mapping system for multi-UAV search and rescue under the forest canopy. Our UAVs were equipped with onboard autonomy that reliably performed sensing, pose estimation, local mapping, and exploration planning. CSLAM was performed at a central ground station. To cope with the limited communication bandwidth, we used a map compression scheme that

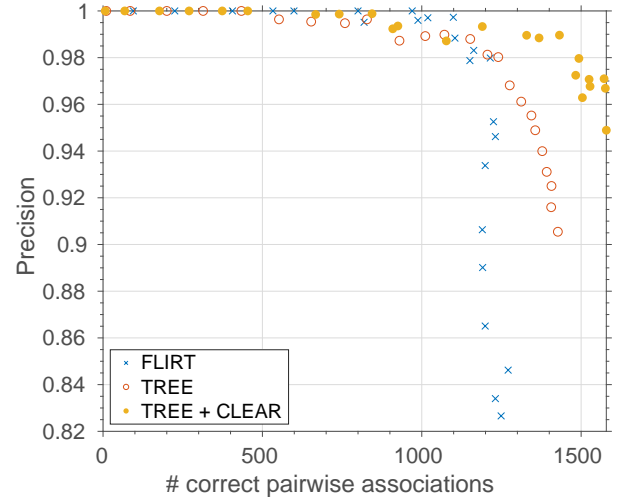


Figure 13. Precision vs. number of correct pairwise associations (unnormalized recall). CG matching with varying tolerance threshold ϵ_{CG} were performed to obtain the data points for FLIRT and trees. Precision is computed as the percentage of correct pairwise associations within all proposed associations. In the forest, the proposed tree detection algorithm unsurprisingly outperformed FLIRT features. Furthermore, CLEAR was able to improve both precision and recall by simultaneously rejecting false associations and suggesting more correct associations.

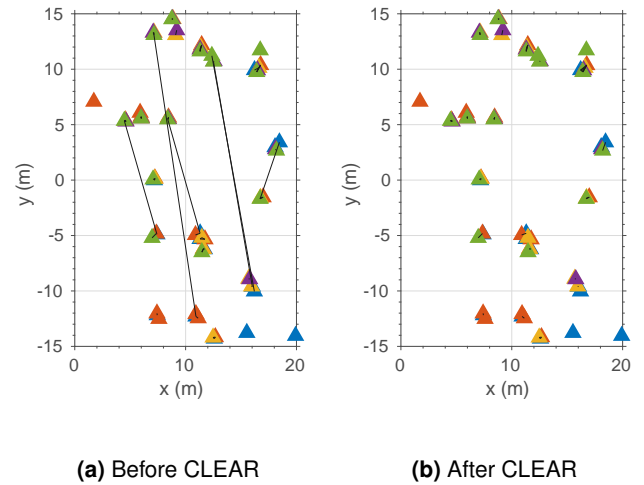


Figure 14. Data association graph before and after optimizing with CLEAR. Each triangle represents a tree colored according to the submap it belongs to. Two trees from different submaps are connected by an edge if they are matched in the given data association. By jointly optimizing over all pairwise matches, CLEAR was able to reject false associations that passed the initial stage of pairwise association.

compressed onboard dense occupancy grids into sparse tree-based maps before transmission. During CSLAM, we used the relative positions and orientations between multiple trees as a unique signature to detect loop closures. To further improve both precision and recall during data association, we proposed cycle consistent multiway matching as an additional stage in our CSLAM pipeline. Extensive experiments were carried out to validate the proposed system, including a real-world flight demonstration at a forest in NASA LaRC.

While the proposed dynamics-aware planner was able to produce smoother and more time efficient search behavior, we observe that its inherent bias to follow the current velocity vector sometimes results in the vehicle flying past a small patch of unobserved space, and having to return later in the mission. An example is shown in Figure 7, where the second vehicle missed the tear-dropped shaped section of unknown space. Possible ways of addressing this problem include encouraging the planner to prioritize small patches of unobserved space (e.g., by clustering frontiers), or incorporating longer-horizon planning during exploration.

Our CSLAM system can also be further improved. In particular, while we could reliably fuse multiple submaps into a consistent object-based map, the fused map nevertheless still contains duplicate objects. This can be seen in Figure 9d, where some overlapping magenta circles most likely correspond to a single tree in the forest. Ideally, we would like to fuse these duplicate landmarks in order to maximize the accuracy of the final map. This can be done by further optimizing upstream modules (e.g., tree detection and pairwise association), or by performing an additional fusion step after landmark SLAM.

Acknowledgements

The authors gratefully acknowledge Chester Dolph, Brian Duvall, and Zak Johns for assistance during the outdoor experiments. The authors also would like to thank Kasra Khosoussi and Kaveh Fathian for insightful discussions during the preparation of this manuscript.

This work was supported in part by the NASA Convergent Aeronautics Solutions project Design Environment for Novel Vertical Lift Vehicles (DELIVER), by ONR under BRC award N000141712072, and by ARL DCIST under Cooperative Agreement Number W911NF-17-2-0181.

References

- Aragues R, Montijano E and Sagues C (2011) Consistent data association in multi-robot systems with limited communications. In: *Robotics: Science and Systems (RSS)*.
- Arandjelović R, Gronat P, Torii A, Pajdla T and Sivic J (2016) NetVLAD: CNN architecture for weakly supervised place recognition. In: *Proceedings of the Conference on Computer Vision and Pattern Recognition (CVPR)*.
- Asmar DC, Zelek JS and Abdallah SM (2006) Tree trunks as landmarks for outdoor vision slam. In: *2006 Conference on Computer Vision and Pattern Recognition Workshop (CVPRW'06)*.
- Aydemir A, Sjöö K, Folkesson J, Pronobis A and Jensfelt P (2011) Search in the real world: Active visual object search based on spatial relations. In: *Proceedings of the International Conference on Robotics and Automation (ICRA)*.
- Bachrach A, Prentice S, He R and Roy N (2011) RANGE—robust autonomous navigation in GPS-denied environments. *Journal of Field Robotics* 28(5): 644–666.
- Bailey T, Nebot EM, Rosenblatt J and Durrant-Whyte HF (2000) Data association for mobile robot navigation: a graph theoretic approach. In: *Proceedings of the International Conference on Robotics and Automation (ICRA)*.
- Bay H, Tuytelaars T and Van Gool L (2006) Surf: Speeded up robust features. In: *Proceedings of the European Conference on Computer Vision (ECCV)*.
- Bircher A, Kamel M, Alexis K, Oleynikova H and Siegwart R (2016) Receding horizon “next-best-view” planner for 3d exploration. In: *Proceedings of the International Conference on Robotics and Automation (ICRA)*.
- Bosse M and Zlot R (2009) Keypoint design and evaluation for place recognition in 2d lidar maps. *Robotics and Autonomous Systems (RAS)*.
- Bourgault F, Makarenko A, Williams S, Grocholsky B and Durrant-Whyte H (2002) Information based adaptive robotic exploration. In: *Proceedings of the International Conference on Intelligent Robots and Systems (IROS)*.
- Calonder M, Lepetit V, Strecha C and Fua P (2010) Brief: Binary robust independent elementary features. In: Daniilidis K, Maragos P and Paragios N (eds.) *Proceedings of the European Conference on Computer Vision (ECCV)*.
- Campbell T, Liu M, Kulis B, How JP and Carin L (2013) Dynamic clustering via asymptotics of the dependent dirichlet process mixture. In: *Advances in Neural Information Processing Systems*, 26.
- Cesare K, Skeeel R, Yoo SH, Zhang Y and Hollinger G (2015) Multi-uav exploration with limited communication and battery. In: *Proceedings of the International Conference on Robotics and Automation (ICRA)*.
- Charrow B, Liu S, Kumar V and Michael N (2015) Information-theoretic mapping using cauchy-schwarz quadratic mutual information. In: *Proceedings of the International Conference on Robotics and Automation (ICRA)*.
- Chen Y, Guibas L and Huang Q (2014) Near-optimal joint object matching via convex relaxation. In: *Proceedings of the International Conference on Machine Learning (ICML)*.
- Chernov N (2010) *Circular and Linear Regression: Fitting Circles and Lines by Least Squares*. Chapman & Hall/CRC Monographs on Statistics & Applied Probability.
- Choudhary S, Carlone L, Nieto C, Rogers J, Christensen HI and Dellaert F (2017) Distributed mapping with privacy and communication constraints: Lightweight algorithms and object-based models. *The International Journal of Robotics Research (IJRR)*.
- Cieslewski T, Choudhary S and Scaramuzza D (2018) Data-efficient decentralized visual SLAM. *Proceedings of the International Conference on Robotics and Automation (ICRA)*.
- Cieslewski T, Kaufmann E and Scaramuzza D (2017) Rapid exploration with multi-rotors: A frontier selection method for high speed flight. In: *Proceedings of the International Conference on Intelligent Robots and Systems (IROS)*.
- Corah M and Michael N (2017) Efficient online multi-robot exploration via distributed sequential greedy assignment. In: *Robotics: Science and Systems (RSS)*.
- Corah M, OMeadhra C, Goel K and Michael N (2019) Communication-efficient planning and mapping for multi-robot exploration in large environments. *IEEE Robotics and Automation Letters (RAL)*.
- Cummins M and Newman P (2011) Appearance-only slam at large scale with FAB-MAP 2.0. *The International Journal of Robotics Research (IJRR)* 30(9): 1100–1123.
- Cunningham A, Indelman V and Dellaert F (2013) Ddf-sam 2.0: Consistent distributed smoothing and mapping. In: *Proceedings*

- of the *International Conference on Robotics and Automation (ICRA)*.
- Cunningham A, Wurm KM, Burgard W and Dellaert F (2012) Fully distributed scalable smoothing and mapping with robust multi-robot data association. In: *Proceedings of the International Conference on Robotics and Automation (ICRA)*.
- Dong J, Nelson E, Indelman V, Michael N and Dellaert F (2015) Distributed real-time cooperative localization and mapping using an uncertainty-aware expectation maximization approach. In: *Proceedings of the International Conference on Robotics and Automation (ICRA)*.
- Dubé R, Cramariuc A, Dugas D, Nieto J, Siegwart R and Cadena C (2018) SegMap: 3d segment mapping using data-driven descriptors. In: *Robotics: Science and Systems (RSS)*.
- Fathian K, Khosoussi K, Lusk P, Tian Y and How JP (2019) Clear: A consistent lifting, embedding, and alignment rectification algorithm for multi-agent data association.
- Feder HJS, Leonard JJ and Smith CM (1999) Adaptive mobile robot navigation and mapping. *The International Journal of Robotics Research, Special Issue on Field and Service Robotics* 18(7): 650–668.
- Fischler MA and Bolles RC (1981) Random sample consensus: A paradigm for model fitting with applications to image analysis and automated cartography .
- Forster C, Lynen S, Kneip L and Scaramuzza D (2013) Collaborative monocular slam with multiple micro aerial vehicles. In: *Proceedings of the International Conference on Intelligent Robots and Systems (IROS)*.
- Gálvez-López D and Tardós JD (2012) Bags of binary words for fast place recognition in image sequences. *IEEE Transactions on Robotics* 28(5): 1188–1197.
- Giamou M, Babich Y, Habibi G and How J (2017) Stable laser interest point selection for place recognition in a forest. In: *Proceedings of the International Conference on Intelligent Robots and Systems (IROS)*.
- Gil A, scar Reinoso, Ballesta M and Juli M (2010) Multi-robot visual slam using a rao-blackwellized particle filter. *Robotics and Autonomous Systems (RAS)* .
- Gonzalez-Baos HH and Latombe JC (2002) Navigation strategies for exploring indoor environments. *The International Journal of Robotics Research (IJRR)* .
- Hart PE, Nilsson NJ and Raphael B (1968) A formal basis for the heuristic determination of minimum cost paths. *IEEE Transactions on Systems Science and Cybernetics* .
- Himstedt M, Frost J, Hellbach S, Böhme HJ and Maehle E (2014) Large scale place recognition in 2D lidar scans using geometrical landmark relations. In: *Proceedings of the International Conference on Intelligent Robots and Systems (IROS)*.
- Hornung A, Wurm KM, Bennewitz M, Stachniss C and Burgard W (2013) Octomap: an efficient probabilistic 3d mapping framework based on octrees. *Autonomous Robots* 34(3): 189–206.
- Huang QX and Guibas L (2013) Consistent shape maps via semidefinite programming. In: *Proceedings of the Eurographics/ACMSIGGRAPH Symposium on Geometry Processing*.
- Indelman V, Nelson E, Michael N and Dellaert F (2014) Multi-robot pose graph localization and data association from unknown initial relative poses via expectation maximization. In: *Proceedings of the International Conference on Robotics and Automation (ICRA)*.
- Jégou H, Douze M, Schmid C and Prez P (2010) Aggregating local descriptors into a compact image representation. In: *Proceedings of the Conference on Computer Vision and Pattern Recognition (CVPR)*.
- Jégou H, Perronnin F, Douze M, Snchez J, Prez P and Schmid C (2012) Aggregating local image descriptors into compact codes. *IEEE Transactions on Pattern Analysis and Machine Intelligence* .
- Jensen EA (2018) Restricted communication in online multi-robot exploration. In: *Proceedings of the Joint Conference on Artificial Intelligence (IJCAI)*.
- Kaess M and Dellaert F (2009) Covariance recovery from a square root information matrix for data association. *Robotics and Autonomous Systems (RAS)* .
- Kaess M, Ranganathan A and Dellaert F (2008) isam: Incremental smoothing and mapping. *IEEE Transactions on Robotics (TRO)* .
- Kallasi F and Rizzini DL (2016) Efficient loop closure based on FALKO lidar features for online robot localization and mapping. In: *Proceedings of the International Conference on Intelligent Robots and Systems (IROS)*.
- Konc J and Janei D (2007) An improved branch and bound algorithm for the maximum clique problem. *MATCH - Communications in Mathematical and in Computer Chemistry* .
- Kukko A, Kaijaluoto R, Kaartinen H, Lehtola VV, Jaakkola A and Hyypä J (2017) Graph slam correction for single scanner mls forest data under boreal forest canopy. *ISPRS Journal of Photogrammetry and Remote Sensing* .
- Leonard J and Feder HJ (2001) Decoupled stochastic mapping. *IEEE Journal of Oceanic Engineering* .
- Leonardos S, Zhou X and Daniilidis K (2017) Distributed consistent data association via permutation synchronization. In: *Proceedings of the International Conference on Robotics and Automation (ICRA)*.
- Lowe DG (2004) Distinctive image features from scale-invariant keypoints. *International Journal of Computer Vision* .
- Mangelson J, Dominic D, Eustice R and Vasudevan R (2018) Pairwise consistent measurement set maximization for robust multi-robot map merging. In: *Proceedings of the International Conference on Robotics and Automation (ICRA)*.
- Meier L, Tanskanen P, Heng L, Lee GH, Fraundorfer F and Pollefeys M (2012) Pixhawk: A micro aerial vehicle design for autonomous flight using onboard computer vision. *Autonomous Robots* 33(1-2): 21–39.
- Mellinger D, Michael N and Kumar V (2012) Trajectory generation and control for precise aggressive maneuvers with quadrotors. *The International Journal of Robotics Research* 31(5): 664–674.
- Montijano E, Aragues R and Sags C (2013) Distributed data association in robotic networks with cameras and limited communications. *IEEE Transactions on Robotics* .
- Morrison JG, Gavez-Lopez D and Sibley G (2016) Scalable multirobot localization and mapping with relative maps: Introducing moarslam. *IEEE Control Systems Magazine* .
- Mur-Artal R and Tardós JD (2017) ORB-SLAM2: an open-source SLAM system for monocular, stereo and RGB-D cameras. *IEEE Transactions on Robotics* .

- Neira J and Tardos JD (2001) Data association in stochastic mapping using the joint compatibility test. *IEEE Transactions on Robotics and Automation*.
- Nguyen A, Ben-Chen M, Welnicka K, Ye Y and Guibas L (2011) An optimization approach to improving collections of shape maps. *Computer Graphics Forum*.
- Öhman M, Miettinen M, Kannas K, Jutila J, Visala A and Forsman P (2008) *Tree Measurement and Simultaneous Localization and Mapping System for Forest Harvesters*.
- Pachauri D, Kondor R and Singh V (2013) Solving the multi-way matching problem by permutation synchronization. In: *Proceedings of the International Conference on Neural Information Processing Systems (NIPS)*.
- Paul R and Newman P (2010) FAB-MAP 3D: Topological mapping with spatial and visual appearance. In: *Proceedings of the International Conference on Robotics and Automation (ICRA)*.
- Paz LM, Pinies P, Neira J and Tardos JD (2005) Global localization in slam in bilinear time. In: *Proceedings of the International Conference on Intelligent Robots and Systems (IROS)*.
- Perronnin F, Liu Y, Snchez J and Poirier H (2010) Large-scale image retrieval with compressed fisher vectors. In: *Proceedings of the conference on Computer Vision and Pattern Recognition (CVPR)*.
- Rublee E, Rabaud V, Konolige K and Bradski G (2011) Orb: An efficient alternative to sift or surf. In: *Proceedings of the International Conference on Computer Vision (ICCV)*.
- Rusu RB, Blodow N and Beetz M (2009) Fast point feature histograms (fpfh) for 3d registration. In: *Proceedings of the International Conference on Robotics and Automation (ICRA)*.
- Saeedi S, Trentini M, Seto M and Li H (2016) Multiple-robot simultaneous localization and mapping: A review. *Journal of Field Robotics (JFR)*.
- Schmuck P and Chli M (2018) CCM-SLAM: Robust and efficient centralized collaborative monocular simultaneous localization and mapping for robotic teams. In: *Journal of Field Robotics (JFR)*.
- Schuster MJ, Schmid K, Brand C and Beetz M (2019) Distributed stereo vision-based 6d localization and mapping for multi-robot teams. *Journal of Field Robotics (JFR)*.
- Singh A, Krause A, Guestrin C and Kaiser WJ (2009) Efficient informative sensing using multiple robots. *Journal of Artificial Intelligence Research*.
- Sturm J, Engelhard N, Endres F, Burgard W and Cremers D (2012) A benchmark for the evaluation of rgb-d slam systems. In: *International Conference on Intelligent Robots and Systems*.
- Tang J, Chen Y, Kukko A, Kaartinen H, Jaakkola A, Khoramshahi E, Hakala T, Hyypä J, Holopainen M and Hyypä H (2015) Slam-aided stem mapping for forest inventory with small-footprint mobile lidar. *Forests*.
- Taubin G (1991) Estimation of planar curves, surfaces, and nonplanar space curves defined by implicit equations with applications to edge and range image segmentation. *IEEE Transactions on Pattern Analysis and Machine Intelligence*.
- Tedrake R (2014) Drake: A planning, control, and analysis toolbox for nonlinear dynamical systems.
- Tian Y, Liu K, Ok K, Tran L, Allen D, Roy N and How J (2018) Search and rescue under the forest canopy using multiple uas. In: *Proceedings of the International Symposium on Experimental Robotics (ISER)*.
- Tipaldi GD and Arras KO (2010) Flirt-interest regions for 2D range data. In: *Proc. ICRA*. pp. 3616–3622.
- Tron R, Zhou X, Esteves C and Daniilidis K (2017) Fast multi-image matching via density-based clustering. In: *IEEE International Conference on Computer Vision (ICCV)*.
- Yamauchi B, Schultz A and Adams W (1998) Mobile robot exploration and map building with continuous localization. In: *Proceedings of the International Conference on Robotics and Automation (ICRA)*.
- Zhou X, Zhu M and Daniilidis K (2015) Multi-image matching via fast alternating minimization. In: *Proceedings of the International Conference on Computer Vision (ICCV)*.
- Zhou XS and Roumeliotis SI (2006) Multi-robot slam with unknown initial correspondence: The robot rendezvous case. In: *Proceedings of the International Conference on Intelligent Robots and Systems (IROS)*.